PHYSICAL REVIEW B **84**, 075136 (2011)

Theory of high-energy optical conductivity and the role of oxygens in manganites

Muhammad Aziz Majidi,[1,4] Haibin Su,[5] Yuan Ping Feng,[1] Michael Rübhausen,[3,1] and Andrivo Rusydi[1,2,3,*]
[1]*NUSNNI-NanoCore, Department of Physics, Faculty of Science, National University of Singapore, Singapore 117542, Singapore*
[2]*Singapore Synchrotron Light Source, National University of Singapore, Singapore 117603, Singapore*
[3]*Institut für Angewandte Physik, Universität Hamburg, Jungiusstrasse 11, D-20355 Hamburg, Germany and*
Center for Free Electron Laser Science (CFEL), Notkestraße 85, D-22607 Hamburg, Germany
[4]*Departemen Fisika, FMIPA, Universitas Indonesia, Depok 16424, Indonesia*
[5]*Division of Materials Science, Nanyang Technological University, 50 Nanyang Avenue, Singapore 639798, Singapore*
(Received 23 July 2010; revised manuscript received 2 January 2011; published 10 August 2011)

Recent experimental study revealed the optical conductivity of $La_{1-x}Ca_xMnO_3$ over a wide range of energy and the occurrence of spectral weight transfer as the system transforms from a paramagnetic insulating to a ferromagnetic metallic phase [A. Rusydi *et al.* Phys. Rev. B **78**, 125110 (2008)]. We propose a model and calculation within the dynamical mean-field theory to explain this phenomenon. We find the role of oxygens in mediating the hopping of electrons between manganeses as the key that determines the structures of the optical conductivity. In addition, by parametrizing the hopping integrals through magnetization, our result suggests a possible scenario that explains the occurrence of spectral weight transfer, in which the ferromagnetic ordering increases the rate of electron transfer from O_{2p} orbitals to upper Mn_{e_g} orbitals while simultaneously decreasing the rate of electron transfer from O_{2p} orbitals to lower Mn_{e_g} orbitals, as temperature is varied across the ferromagnetic transition. With this scenario, our optical conductivity calculation shows very good quantitative agreement with the experimental data.

DOI: 10.1103/PhysRevB.84.075136 PACS number(s): 78.20.Bh, 71.10.−w, 71.30.+h, 71.20.−b

I. INTRODUCTION

Manganites have been the subject of extensive studies because they have exhibited a wealth of fascinating phenomena, such as colossal magnetoresistance (CMR); charge, spin, and orbital orderings; the ability to transition from a paramagnetic insulator to a ferromagnetic metal; and multiferroic behavior.[1–4] Upon hole doping, the transition from an antiferromagnetic insulator to a ferromagnetic metal has been argued to occur through a mixed-phase process,[5] whereas for a fixed hole doping where ferromagnetic order is found, an insulator to metal transition occurs simultaneously as the temperature is lowered across the ferromagnetic transition.[6] It has been generally assumed and experimentally confirmed that the magnetic order in these systems is driven by double-exchange interactions.[5,7–11] However, the explanation of the other phenomena accompanying the ferromagnetic transition seems to be far from complete, and remains an open subject.

Several theories on the insulator-metal (IM) transition that accompanies the ferromagnetic transition have been proposed.[12,13] Although the details of the models and scenarios of the IM transition proposed by these theories are quite different, they have similar ideas suggesting that the Jahn-Teller (JT) distortion along with the electron-phonon interactions stabilize the insulating phase at high temperatures; this phase is broken by the ferromagnetic order below its transition temperatures. These theories, however, have only addressed the static properties or low-energy phenomena, as their models implicitly assume that low-energy phenomena occurring in these materials are insensitive to possible high-energy excitations. Many such models[14–19] typically consider only effective hoppings between Mn sites while ignoring the electronic states in oxygen sites. On the other hand, models that include local interactions and hybridization in correlated materials might expect pronounced effects at higher energies that are connected to charge-transfer or Mott-Hubbard physics.[20–23] Thus, the validity of such theories may have to be tested through experimental studies on the band structures and the optical properties over a wide range of energy. In that respect, experimental studies of optical conductivity of manganites as functions of temperature and doping in a much wider energy range become crucial.

A recent study of optical conductivity done by Rusydi *et al.*[24] revealed for the first time strong temperature and doping dependences in $La_{1-x}Ca_xMnO_3$ for $x = 0.3$ and 0.2. The occurrence of spectral weight transfer has been strikingly found between low (<3 eV), medium (3–12 eV), and high energies (>12 eV) across the IM transition. In fact, as the temperature is decreased, the spectral weight transfer appears more noticeably in the medium- and high-energy regions than it does in the low-energy region. Observing how the spectral weight in each region of energy simultaneously changes as temperature is decreased passing the ferromagnetic (FM) transition temperature (T_{FM}), one may suspect that there is an interplay between low-, medium-, and high-energy charge transfers that may drive many phenomena occurring in manganites, including the IM transition. This conjecture is related to the fact that the hopping of an electron from one Mn site to another can only occur through an O site.

Considering the difference between the on-site energy of the manganese and that of the oxygen, which could be about 5–8 eV,[25] the Mn-O hoppings occur with high-energy transfer. We hypothesize that if such high-energy hoppings can mediate a ferromagnetic order, then other low- or high-energy phenomena may occur simultaneously. Thus, the mechanism of IM transition in the dc conductivity may not be completely separated from what appears as the decrease (increase) of the spectral weight in the medium- (high-) energy region of the optical conductivity, all of which may be driven by the ferromagnetic ordering. Theories based on effective low-energy models that only consider Mn sites while ignoring O sites would not be able to address this.

Motivated by the aforementioned conjecture, we develop a simple but more general model, in which oxygens are explicitly incorporated. In this paper, we propose our model and calculation of the optical conductivity of $La_{1-x}Ca_xMnO_3$ within the dynamical mean-field theory to explain the experimental results of Ref. 24. Our calculated optical conductivity shows that both oxygens and manganeses play important roles in forming structures similar to those of the experimental results. Further, with some additional argument, our calculation captures qualitatively correctly the temperature dependence of the optical conductivity as the system transforms from paramagnetic to ferromagnetic phase.

II. MODEL

As shown in Fig. 1, we model the crystal structure of $La_{1-x}Ca_xMnO_3$ such that each unit cell forms a cube with lattice constant a set equal to 1, and contains only one Mn and three O sites, thus ignoring the presence of La and Ca atoms that we believe not to contribute much to the structures and temperature dependence of the optical conductivity. We choose 10 basis orbitals to construct our Hilbert space, which we order as follows: $|\mathrm{Mn}e_{g\ \mathrm{upper},\uparrow}\rangle$, $|\mathrm{Mn}e_{g\ \mathrm{lower},\uparrow}\rangle$, $|\mathrm{O}_1 p_\uparrow\rangle$, $|\mathrm{O}_2 p_\uparrow\rangle$, $|\mathrm{O}_3 p_\uparrow\rangle$, $|\mathrm{Mn}e_{g\ \mathrm{upper},\downarrow}\rangle$, $|\mathrm{Mn}e_{g\ \mathrm{lower},\downarrow}\rangle$, $|\mathrm{O}_1 p_\downarrow\rangle$, $|\mathrm{O}_2 p_\downarrow\rangle$, and $|\mathrm{O}_3 p_\downarrow\rangle$. Note that the distinction between $|e_{g\ \mathrm{upper}}\rangle$ and $|e_{g\ \mathrm{lower}}\rangle$ states is associated with the Jahn-Teller splitting. Using this set of bases, we propose a Hamiltonian:

$$H = \frac{1}{N}\sum_{\mathbf{k}} \eta_{\mathbf{k}}^{\dagger}[H_0(\mathbf{k})]\eta_{\mathbf{k}} + \sum_{i,\sigma,\sigma'} U n_{u_i\sigma} n_{l_i\sigma'} + \sum_i U_u n_{u_i\uparrow} n_{u_i\downarrow} + \sum_i U_l n_{l_i\uparrow} n_{l_i\downarrow} - \sum_i J_H \mathbf{S}_i . \mathbf{s}_i . \tag{1}$$

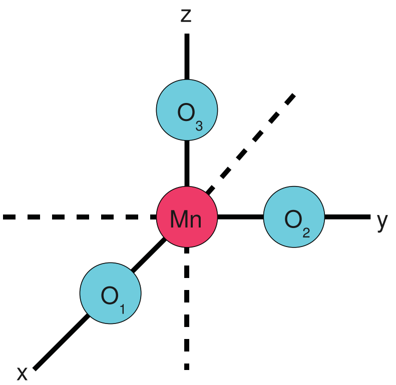

FIG. 1. (Color online) Simplified crystal structure of the model. The crystal structure is assumed cubic with the unit cell containing only one Mn and three O atoms. The O atoms are labeled 1, 2, and 3 to distinguish the p orbitals belonging to different O atoms used to construct our Hamiltonian.

The first term in the Hamiltonian is the kinetic part, whereof $\eta_{\mathbf{k}}^{\dagger}$ is a row vector whose elements are the creation operators associated with the 10 basis orbitals, and $\eta_{\mathbf{k}}$ is its Hermitian conjugate containing the corresponding destruction operators. Here we consider that each Mn site contributes four e_g orbitals (the upper and lower of each of which is with up and down spins), and the three O sites contribute six orbitals (three from each site, each of which is with up and down spins). $[H_0(\mathbf{k})]$ is a 10×10 matrix in momentum space whose structure is arranged in four 5×5 blocks corresponding to their spin directions as

$$[H_0(\mathbf{k})] = \begin{bmatrix} H_0(\mathbf{k})_\uparrow & \mathbf{O} \\ \mathbf{O} & H_0(\mathbf{k})_\downarrow \end{bmatrix}, \tag{2}$$

where $\mathbf{O}$ is a zero matrix of size 5×5, and (referring to the choice of coordinates in Fig. 1)

$$H_0(\mathbf{k})_{\uparrow(\downarrow)} = \begin{bmatrix} E_{\mathrm{JT}} & 0 & t^{(1)}_{\text{Mn-O}}(1+e^{-ik_x}) & t^{(1)}_{\text{Mn-O}}(1+e^{-ik_y}) & t^{(1)}_{\text{Mn-O}}(1+e^{-ik_z}) \\ 0 & -E_{\mathrm{JT}} & t^{(2)}_{\text{Mn-O}}(1+e^{-ik_x}) & t^{(2)}_{\text{Mn-O}}(1+e^{-ik_y}) & t^{(2)}_{\text{Mn-O}}(1+e^{-ik_z}) \\ t^{(1)}_{\text{Mn-O}}(1+e^{ik_x}) & t^{(2)}_{\text{Mn-O}}(1+e^{ik_x}) & E_p & t_{\text{O-O}}(1+2e^{ik_x}+2e^{-ik_y}) & t_{\text{O-O}}(1+2e^{ik_x}+2e^{-ik_z}) \\ t^{(1)}_{\text{Mn-O}}(1+e^{ik_y}) & t^{(2)}_{\text{Mn-O}}(1+e^{ik_y}) & t_{\text{O-O}}(1+2e^{-ik_x}+2e^{ik_y}) & E_p & t_{\text{O-O}}(1+2e^{ik_y}+2e^{-ik_z}) \\ t^{(1)}_{\text{Mn-O}}(1+e^{ik_z}) & t^{(2)}_{\text{Mn-O}}(1+e^{ik_z}) & t_{\text{O-O}}(1+2e^{-ik_x}+2e^{ik_z}) & t_{\text{O-O}}(1+2e^{-ik_x}+2e^{ik_z}) & E_p \end{bmatrix}. \tag{3}$$

The diagonal elements of $H_0(\mathbf{k})_{\uparrow(\downarrow)}$ represent the local energies, while the off-diagonal elements represent the hybridizations between orbitals. The first two diagonal elements, that is, E_{JT} and $-E_{\mathrm{JT}}$, correspond to the Mn_{e_g} orbital energies, which are split due to the presumedly static Jahn-Teller distortion. Each of the remaining three diagonal elements, that is, E_p, corresponds to the local energy of the O_{2p} orbital. The parameter $t^{(1)}_{\text{Mn-O}}$ ($t^{(2)}_{\text{Mn-O}}$) corresponds to hopping between the upper (lower) Mn_{e_g} orbital and the nearest O_{2p} orbital, whereas $t_{\text{O-O}}$ corresponds to hopping between the nearest O_{2p} orbitals.

The second term in Eq. (1) represents the Coulomb repulsions between the upper and lower Mn_{e_g} orbitals in a site. The third and fourth terms represent the intraorbital Coulomb repulsions. In this work, we take U_u and U_l to be infinity, forbidding double occupancy in each of the lower and upper Mn$_{e_g}$ orbitals. Finally, the fifth term represents the double-exchange magnetic interactions between the local spins of Mn, **S**, formed by the strong Hund's coupling among three t_{2g} electrons giving $S = 3/2$, and the itinerant spins of the upper and lower Mn$_{e_g}$ electrons, **s**. Note that we use a well-accepted general assumption that the on-site Coulomb repulsion in each t_{2g} orbital and the Hund's coupling among the t_{2g} orbitals are strong enough to keep the occupancy of the three t_{2g} levels fixed at high spin configuration. Thus the charge degrees of freedom of the three t_{2g} electrons become frozen, and the remaining degree of freedom to be considered is the orientation of the collective spin 3/2.

III. METHOD

To solve our model, we use the dynamical mean-field theory.[26] First, we define the Green function of the system, which is a 10×10 matrix,

$$[G(\mathbf{k},z)] = \{z[I] - [H_0(\mathbf{k})] - [\Sigma(z)]\}^{-1}, \tag{4}$$

with z the frequency variable and $[I]$ the 10×10 unit matrix. Then, we coarse-grain it over the Brillouin zone as

$$[G(z)] = \frac{1}{N}\sum_{\mathbf{k}}[G(\mathbf{k},z)]. \tag{5}$$

In defining $[G(\mathbf{k},z)]$, all the interaction parts of the Hamiltonian (all terms other than the kinetic part) are absorbed into a momentum-independent self-energy matrix, $[\Sigma(z)]$, which will be solved self-consistently. Note that in this algorithm, we need to go over the self-consistent loops in both Matsubara ($z = i\omega_n + \mu$) and real frequency ($z = \omega + i0^+$).

On taking U_u and U_l to be infinity, to some approximation, we forbid the double occupancies in states $|\mathrm{Mn}e_{g\ \mathrm{upper},\uparrow}\rangle$, $|\mathrm{Mn}e_{g\ \mathrm{lower},\uparrow}\rangle$, $|\mathrm{Mn}e_{g\ \mathrm{upper},\downarrow}\rangle$, and $|\mathrm{Mn}e_{g\ \mathrm{lower},\downarrow}\rangle$ by throwing them out of our Hilbert space. To do this, according to the structure of Hamiltonian matrix in Eqs. (2) and (3), we multiply the weights of all the diagonal elements with indices 1, 2, 6, and 7, and all the corresponding off-diagonal elements connecting any pair of them by a half. Thus, after obtaining the matrix $[G(z)]$ from Eq. (5), the effective $[G(z)]$ (let us call it $[G(z)]_{\mathrm{eff}}$) can be obtained by multiplying each of the following blocks of $[G(z)]$ by a half, while keeping the remaining elements unchanged, that is

$$\begin{aligned}
\begin{bmatrix} G_{11} & G_{12} \\ G_{21} & G_{22} \end{bmatrix} &\Rightarrow \frac{1}{2}\begin{bmatrix} G_{11} & G_{12} \\ G_{21} & G_{22} \end{bmatrix},\\
\begin{bmatrix} G_{16} & G_{17} \\ G_{26} & G_{27} \end{bmatrix} &\Rightarrow \frac{1}{2}\begin{bmatrix} G_{16} & G_{17} \\ G_{26} & G_{27} \end{bmatrix},\\
\begin{bmatrix} G_{61} & G_{62} \\ G_{71} & G_{72} \end{bmatrix} &\Rightarrow \frac{1}{2}\begin{bmatrix} G_{61} & G_{62} \\ G_{71} & G_{72} \end{bmatrix},\\
\begin{bmatrix} G_{66} & G_{67} \\ G_{76} & G_{77} \end{bmatrix} &\Rightarrow \frac{1}{2}\begin{bmatrix} G_{66} & G_{67} \\ G_{76} & G_{77} \end{bmatrix}.
\end{aligned} \tag{6}$$

The "mean-field" Green function can then be extracted as

$$[\mathcal{G}(z)] = \left\{[G(z)]_{\mathrm{eff}}^{-1} + [\Sigma(z)]\right\}^{-1}. \tag{7}$$

Next, we construct the local self-energy matrix, $[\Sigma_{n_l}(z)]$, corresponding to the second and the fifth terms of the Hamiltonian. Here $n_l \in \{0,1\}$ is the occupation number of the lower Mn$_{e_g}$ orbital. The elements of the 10×10 matrix $[\Sigma_{n_l}(z)]$ are all zero except for the blocks,

$$\begin{aligned}
&\begin{bmatrix} \Sigma_{11} & \Sigma_{16} \\ \Sigma_{61} & \Sigma_{66} \end{bmatrix}\\
&\quad = \begin{bmatrix} -J_H S\cos\theta + n_l U & -J_H S\sin\theta(\cos\phi + i\sin\phi) \\ -J_H S\sin\theta(\cos\phi - i\sin\phi) & J_H S\cos\theta + n_l U \end{bmatrix},\\
&\begin{bmatrix} \Sigma_{22} & \Sigma_{27} \\ \Sigma_{72} & \Sigma_{77} \end{bmatrix}\\
&\quad = \begin{bmatrix} -J_H S\cos\theta & -J_H S\sin\theta(\cos\phi + i\sin\phi) \\ -J_H S\sin\theta(\cos\phi - i\sin\phi) & J_H S\cos\theta \end{bmatrix},
\end{aligned} \tag{8}$$

where θ and ϕ are the corresponding angles representing the direction of **S** in the spherical coordinate. The local interacting Green function matrix is then calculated through

$$\left[G_{n_l}(z)\right] = \left\{[\mathcal{G}(z)]^{-1} - \left[\Sigma_{n_l}(z)\right]\right\}^{-1}. \tag{9}$$

For each Mn site with a given n_l, the probability of Mn spin **S** having a direction with angle θ with respect to the direction of magnetization (which is defined as the z axis) is given by

$$P_{n_l}(\cos\theta) = \frac{e^{-S_{n_l}(\cos\theta)}}{Z_{n_l}}, \tag{10}$$

where

$$Z_{n_l} = \int d(\cos\theta)\, e^{-S_{n_l}(\cos\theta)} \tag{11}$$

is the local partition function, and

$$S_{n_l}(\cos\theta) = -\sum_n \ln\det\left[G_{n_l}(i\omega_n)\right]e^{i\omega_n 0^+} \tag{12}$$

is the effective action.

We need to average $[G_{n_l}(z)]$ over all possible θ and n_l values as

$$\begin{aligned}
[G(z)]_{\mathrm{av}} = (1 - \langle n_l\rangle)&\int d(\cos\theta)P_0(\cos\theta)[G_0(z)]\\
&+\langle n_l\rangle\int d(\cos\theta)P_1(\cos\theta)[G_1(z)],
\end{aligned} \tag{13}$$

where $\langle n_l\rangle$ is the average occupation of lower the Mn$_{e_g}$ orbital. The new self-energy matrix is extracted through

$$[\Sigma(z)] = [\mathcal{G}(z)]^{-1} - [G(z)]_{\mathrm{av}}^{-1}. \tag{14}$$

Finally, we feed this new self-energy matrix back into the definition of Green function in Eq. (4), and the iteration process continues until $[\Sigma(z)]$ converges.

After the self-consistency is achieved, we can compute the density of states as

$$\mathrm{DOS}(\omega) = -\frac{1}{\pi}\mathrm{Im}\mathrm{Tr}[G(\omega + i0^+)]. \tag{15}$$

We can also compute the optical conductivity tensor as

$$\sigma_{\alpha\beta}(\omega) = \frac{\pi e^2}{\hbar a d}\int d\nu \left(\frac{f(\nu,T) - f(\nu+\omega,T)}{\omega}\right) \times \frac{1}{N}\sum_{\mathbf{k}} \mathrm{Tr}[v_\alpha(\mathbf{k})][A(\mathbf{k},\nu)][v_\beta(\mathbf{k})][A(\mathbf{k},\nu+\omega)], \tag{16}$$

where $[v_\lambda(\mathbf{k})] = \partial[H_0(\mathbf{k})]/\partial k_\lambda$ is the Cartesian component of the velocity matrix, $[A(\mathbf{k},\nu)] = \{[G(\mathbf{k},\omega + i0^+)] - [G(\mathbf{k},\omega - i0^+)]\}/(2\pi i)$ is the spectral function matrix, and $f(\nu,T)$ is the Fermi distribution function. Note that the dimensional prefactor $\pi e^2/(\hbar a d)$[26] with $d = 3$ and $a = 3.3945$ Å[25] is introduced to restore the proper physical unit, since the rest of the expression was derived by setting $e = \hbar = a = 1$. In our model, the system is isotropic, and we are only interested in the longitudinal components $\sigma_{\alpha\alpha}(\omega) \equiv \sigma(\omega)$, which are equal for all $\alpha \in \{x,y,z\}$.

IV. RESULTS

Our calculated DOS is shown in Fig. 2. The parameter values used for this calculation are $E_{\mathrm{JT}} = 0.5$ eV, $E_p = -6.5$ eV, $t^{(1)}_{\text{Mn-O}} = 1.2$ eV, $t^{(2)}_{\text{Mn-O}} = 0.8$ eV, $t_{\text{O-O}} = 0.6$ eV, $U = 10$ eV, $J_H = 1.5$ eV, and $T \approx 194$ K (corresponding to $\beta \equiv 1/T = 60$ eV^{-1}). These parameter values are chosen considering rough estimates given in other papers[12,13,25] and adjusted so as to give best agreement with the experimental optical conductivity data in Ref. 24. The DOS is normalized such that the integrated area is equal to 8, since in each unit cell there are six orbitals coming from oxygens and effectively two from manganeses, considering the restriction given by relation (6). The chemical potential is self-consistently adjusted to satisfy the electron filling of $6 + (1 - x) = 6.7$, mimicking the situation of La$_{1-x}$Ca$_x$MnO$_3$ for $x = 0.3$. The structures of the DOS can be explained as follows. The three peaks labeled 1,2,3 result from the fact that there are three oxygen atoms in a unit cell, where the degeneracy is broken into three levels by the hybridization between $2p$ orbitals of the neighboring oxygen atoms. The structures labeled 4 through 9 result from the e_g orbitals of manganeses. As shown in the figure, there are three mechanisms that split the Mn$_{e_g}$ states into six levels: static JT distortion, Coulomb repulsion (U_{eff}) between lower and upper JT-split e_g states, and the double-exchange (DE) interaction between spins of electrons in the lower and upper JT-split states and the Mn spins formed by the Hund's coupling among the Mn t_{2g} electrons.[27]

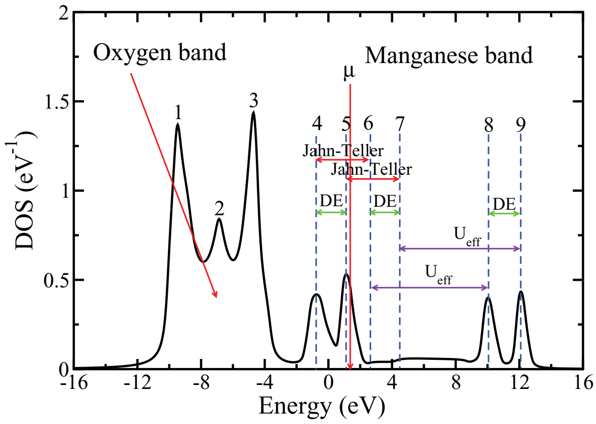

FIG. 2. (Color online) Calculated density of states (DOS). See text for the parameter values used in this figure and the detailed explanation of the structures of the DOS.

Figure 3 shows our calculated optical conductivity for $T \approx 194$ K ($> T_{\mathrm{FM}}$). The ferromagnetic transition temperature for this set of parameters is roughly $T_{\mathrm{FM}} \approx 160$ K (based on extrapolation of the mean-field trend). The parameter values for $T \approx 194$ K are the same as those used in Fig. 2. In Fig. 3, we demonstrate how we tune the profile of the optical conductivity to achieve the best resemblance with the experimental data in Ref. 24. It is important to note that our model is not meant to address the dc conductivity, as we already anticipate that it cannot form an insulating (or nearly insulating) phase at $T > T_{\mathrm{FM}}$, possibly due to not incorporating electron-phonon interactions.[12,13,28] Rather, our goal is to show how this simple model can capture qualitatively the general profile of the optical conductivity from about 1 eV away from the Drude peak up to 22 eV (the energy limit of the experimental data).

On calculating the optical conductivity from Eq. (16), we introduce an imaginary self-energy for the O$_{2p}$ states, $-i\Gamma$, where $\tau = 1/\Gamma$ corresponds to the lifetime of the O$_{2p}$ states. The red curve in Fig. 3 shows the result if we use the self-consistent chemical potential, μ, in Eq. (16). Here, we observe that the resulting profile around the medium-energy region (≈5–11 eV) does not satisfactorily resemble that of the experimental data in Ref. 24, since some spectral weight seems to be missing in that region. We argue that the reason for this is related to the fact that our self-consistent chemical potential, μ, does not lie inside a pseudogap as it probably would if

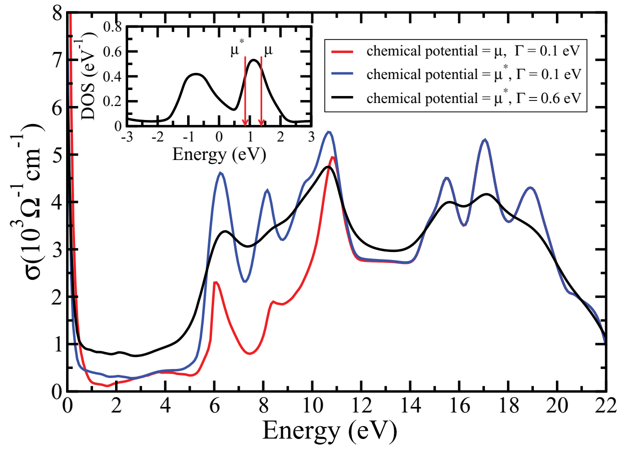

FIG. 3. (Color online) Calculated optical conductivity. Main panel: The red and blue curves represent the calculated optical conductivities for different positions of the chemical potential, μ and μ^*, respectively, using only a small broadening ($\Gamma = 0.1$ eV). The black curve represents the result using the chemical potential at μ^* with a bigger broadening ($\Gamma = 0.6$ eV). Inset: Region in the density of states showing how the position of the chemical potential is shifted. See text for a detailed explanation.

we incorporated electron-phonon interactions. In this model, we only have a pseudogap that results from the DE splitting, where μ falls slightly to the right outside of this pseudogap. To remedy the missing spectral weight, we shift the position of the chemical potential slightly to the left, that is, from μ to μ^*, as shown in the inset of Fig. 3. Using this new chemical potential, μ^*, the resulting optical conductivity, shown by the blue curve, resembles the experimental data better. This suggests that the true chemical potential may actually lie inside a pseudogap similar to the situation when it lies at μ^*. (Note that, as long as we consider the optical conductivity region about 1 eV away from the Drude peak, choosing μ^* between 0.1 and 0.9 eV, that is, around the valley, leads to similar results.) Although the profile of the blue curve is already better than the red one, it still has more pronounced structures than the actual experimental data. To further tune the calculated optical conductivity to better resemble the experimental data, we find that the overly pronounced structures can be broadened by enlarging the O_{2p} imaginary self-energy up to $\Gamma = 0.6$ eV. The result after the broadening, which is shown by the black curve, looks very similar to the experimental results shown in Fig. 2(b) of Ref. 24 (replotted in the inset of Fig. 4). This similarity in both magnitude and profile of the energy dependence may be a good measure of the validity of our model.

Now we discuss how the model captures the spectral weight transfer when temperature is decreased from $T > T_{\mathrm{FM}}$ to $T < T_{\mathrm{FM}}$. First, we divide the energy range into three regions: I (low: $\approx$ 1–3 eV), II (medium: $\approx$3–12 eV), and III (high: $\gtrsim$ 12 eV), following the division made for the experimental data in Ref. 24, except that we exclude the region around the Drude peak from our discussion, since to obtain the correct values of conductivity in that region requires a more accurate description of the renormalized band structure around the chemical potential. If we decrease the temperature from the paramagnetic to the ferromagnetic phase while keeping all the parameters constant, we find no significant change in the optical conductivity, thus the spectral weight transfer does not occur in this way. If we inspect how Eq. (16) determines the optical conductivity, we see that the change in optical conductivity may become more significant if either the spectral function, $[A(\mathbf{k},\nu)]$, or the velocity operator, $[v_\alpha(\mathbf{k})]$, changes significantly while temperature changes. Within our model, this can only be accommodated if we allow some parameters to depend on temperature in some manner. By comparing the structures of optical conductivity and the corresponding DOS profile, it is clear that the spectral weight in the medium-energy region comes mostly from transitions from O_{2p} to lower Mn_{e_g} states, while in the high-energy region it comes from O_{2p} to upper Mn_{e_g} states. This fact may suggest that the hopping parameters $t^{(1)}_{\text{Mn-O}}$ and $t^{(2)}_{\text{Mn-O}}$ depend on temperature. Furthermore, since the spectral weight transfer occurs most notably across and below T_{FM}, the temperature dependence of $t^{(1)}_{\text{Mn-O}}$ and $t^{(2)}_{\text{Mn-O}}$ may be related to spin correlation.

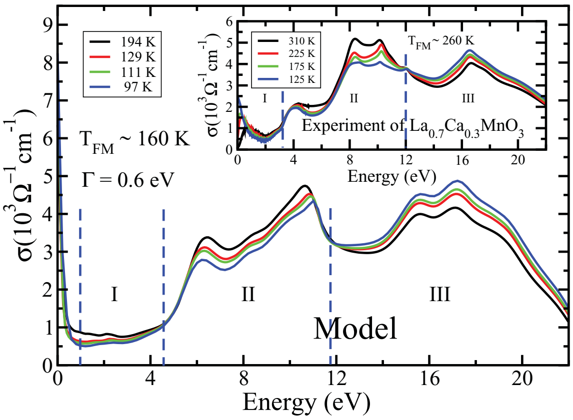

FIG. 4. (Color online) Spectral weight transfer in the optical conductivity. Main panel: Results of the model. Excluding the region containing the Drude peak (0–1 eV), the energy range is divided into three regions: I, II, and III. The black curve represents the optical conductivity in the paramagnetic phase, while the red, green, and blue curves correspond successively to lower temperatures in the ferromagnetic phase.[29] The borders between regions I–II and II–III, denoted by the blue vertical dashed lines, are defined such that the curves are crossing at these energies. Inset: A replot of the corresponding experimental data from Ref. 24 for comparison.

The actual interplay resulting in such a temperature dependence is believed to be very complicated, since it may involve orbital effects on the dynamic electron-phonon coupling and spin correlation. In that regard, our present model, which is not an *ab initio* based model, cannot naturally capture these temperature effects. Thus, to capture the plausible physics within our present model, we turn to the phenomenological approach by parametrizing the totally nontrivial temperature effects on hopping integrals through magnetization. In the simplest level, we may assume a linear dependence of the hopping integrals $t^{(1)}_{\text{Mn-O}}$ and $t^{(2)}_{\text{Mn-O}}$ on the magnetization. Hence, we may write

$$t^{(1)}_{\text{Mn-O}}(M) = t^{(1)}_{\text{Mn-O}}(0)\left(1 + c_1\frac{M}{M_s}\right), \tag{17}$$

$$t^{(2)}_{\text{Mn-O}}(M) = t^{(2)}_{\text{Mn-O}}(0)\left(1 + c_2\frac{M}{M_s}\right), \tag{18}$$

where M/M_s is the ratio of magnetization to the saturated magnetization, and c_1, and c_2 are constants.

Using relations (17) and (18), taking $t^{(1)}_{\text{Mn-O}}(0) = 1.2$ eV, $t^{(2)}_{\text{Mn-O}}(0) = 0.8$ eV, $c_1 \approx 0.23$, and $c_2 \approx -0.35$ at $T = 97$ K, for which $M/M_s = 0.357$, for instance, we obtain that $t^{(1)}_{\text{Mn-O}}$ is enhanced to be $\approx$1.3 eV, while $t^{(1)}_{\text{Mn-O}}$ is suppressed to be $\approx$0.7 eV. The results for four different temperatures are shown in Fig. 4. As shown in the main panel, our calculation shows that the spectral weight simultaneously decreases (increases) in the medium (high) -energy region of the optical conductivity as the system becomes ferromagnetic.[30] Our calculation also produces a less noticeable decrease of the spectral weight in the low-energy region as observed in the experimental data (see the inset). In both the main panel and the inset, the black curve represents the optical conductivity in the paramagnetic phase, while the red, green, and blue curves correspond successively to lower temperatures in the ferromagnetic phase. If we define the positions of the borders between energy regions I–II and II–III such that all the curves are crossing at these energies, we conclude that the theoretical values of these energies are similar to the experimental ones. Note that the temperatures that were varied in the theoretical and the experimental results should not be compared quantitatively, since the theoretical $T_{\rm FM}$ is about 100 K too small compared to the experimental one, possibly due to neglecting other possible exchange interactions in our model. Despite this, we believe that any improvement of $T_{\rm FM}$ by such additional terms would not change the physics presented in this paper. To show the difference in the DOS between paramagnetic and ferromagnetic phases, we display the spin-dependent DOS for $T \approx 194$ K and $T \approx 97$ K in Fig. 5.

To demonstrate further how the spectral weight transfers in our model compare with the experimental results, we display the relative spectral weight changes for different regions of energy in Fig. 6. Comparing results in Figs. 6(a) and 6(b), it is clear that for every region of energy—I (low), II (medium), and III (high) (excluding 0–1 eV)—our calculations give exactly the same trends as those shown by the experimental results. This suggests that the ingredients incorporated in our model are adequate to explain the occurrence of spectral weight transfers in $\mathrm{La}_{1-x}\mathrm{Ca}_x\mathrm{MnO}_3$ in the energy range up to 22 eV. In that respect, one may argue, for instance, that the high-spin state ($S = 3/2$) of the t_{2g} electrons may become unstable as the system is optically excited by high-energy photons. Accordingly, transitions from high- to low-spin states, or excitations of electrons from the t_{2g} to the e_g levels, may occur. Our present model does not incorporate those possibilities. However, our calculations prove that the model is capable of obtaining the spectral weight transfers with good qualitative agreement with the experimental results, thus suggesting that such other contributions may be minor or irrelevant.

The inset of Fig. 6(a) shows that for the 0–1 eV region, our result does not agree with the experiment, since it does not capture the insulator-metal transition. As mentioned earlier, we argue that this is due to our model not incorporating the dynamic Jahn-Teller phonons and their interactions with electrons, which may be responsible for forming an insulating gap in the paramagnetic phase. The incorporation of such terms to improve our present model is under ongoing study.

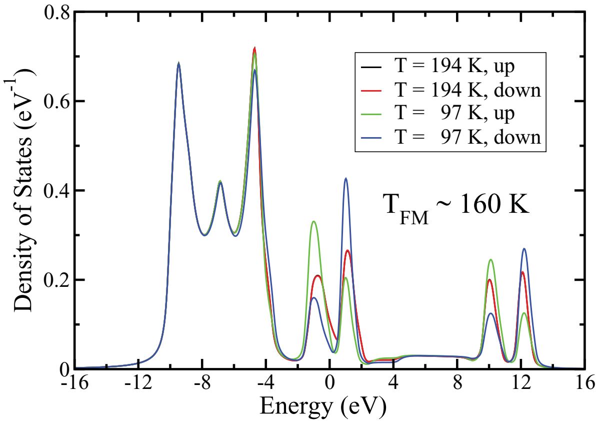

FIG. 5. (Color online) Spin-dependent density of states. The black and red curves lie on top of each other as the spin-up and spin-down components of the DOS are identical in the PM phase, while the green and blue curves look quite distinct as the DOS becomes polarized in the FM phase.

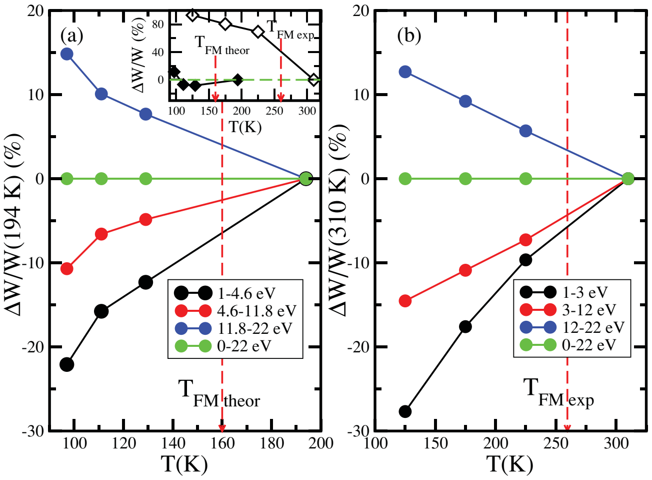

FIG. 6. (Color online) Relative spectral-weight changes. $\Delta W(T)/W$ from (a) our calculations and (b) the experimental results of Ref. 24, for different regions of energy. $\Delta W/W$ is defined as the spectral-weight difference $\Delta W = \int_{\omega_1}^{\omega_2}[\sigma(\omega,T) - \sigma(\omega,T_{\rm PM})]d\omega$ normalized to $W(T_{\rm PM}) = \int_{\omega_1}^{\omega_2}\sigma(\omega,T_{\rm PM})d\omega$, where in this case $T_{\rm PM}$ is 194 K in (a) and 310 K in (b). Positions of the theoretical and the experimental $T_{\rm FM}$ are indicated by vertical red dashed lines in each panel. The inset in (a) is a comparison between $\Delta W(T)/W$ from the calculations (black filled diamonds) and from the experiments of Ref. 24 (black empty diamonds) for the 0–1 eV region. The horizontal green dashed line in the inset is just to highlight the zero position of $\Delta W/W$.

V. CONCLUSION

In conclusion, we have developed a model to explain the structures and the spectral weight transfer occurring in the optical conductivity of $\mathrm{La}_{1-x}\mathrm{Ca}_x\mathrm{MnO}_3$ for $x = 0.3$. The key that makes our model work in capturing the structures of the optical conductivity at medium and high energies is the inclusion of O_{2p} orbitals into the model.

Further, by parametrizing the hopping integrals through magnetization, our model captures the spectral weight transfer as temperature is decreased across the ferromagnetic transition temperature. Our calculation based on these phenomenological parameters suggests that the ferromagnetic ordering increases the hopping parameter connecting the O_{2p} orbitals and the upper Mn_{e_g} orbitals, while simultaneously decreasing the hopping parameter connecting the O_{2p} orbitals and the lower Mn_{e_g} orbitals. Although we have yet to check whether this scenario works in a more complete model incorporating the dynamic electron-phonon coupling, we conjecture that this may be an important part that contributes to the mechanism of insulator to metal transition in manganites.

Overall, our results demonstrate the strength of our model, which one may have to consider as the minimum model before adding other ingredients to properly explain the insulator-metal transition or other features in correlated electron systems such as manganites.

ACKNOWLEDGMENTS

M.A.M. and A.R. thank George Sawatzky and Seiji Yunoki for their valuable comments and suggestions. This work is supported by NRF-CRP grant "Tailoring Oxide Electronics by Atomic Control," No. NRF2008NRF-CRP002-024, NUS YIA, an NUS cross faculty grant, and FRC. We acknowledge the CSE-NUS computing center for providing facilities for our numerical calculations. Work at NTU was supported in part by a MOE AcRF Tier-1 grant (Grant No. M52070060).

---

*phyandri@nus.edu.sg

[1] S. Jin, T. H. Tiefel, M. McCormack, R. A. Fastnacht, R. Ramesh, and L. H. Chen, Science **264**, 413 (1994).

[2] For a general review on the structure and transport in manganites, see M. B. Salamon and M. Jaime, Rev. Mod. Phys. **73**, 583 (2001), and references therein.

[3] S.-W. Cheong and M. Mostovoy, Nat. Mater. **6**, 13 (2007).

[4] E. Saitoh, S. Okamoto, K. T. Takahashi, K. Tobe, K. Yamamoto, T. Kimura, S. Ishihara, S. Maekawa, and Y. Tokura, Nature (London) **410**, 180 (2001).

[5] A. Moreo, S. Yunoki, and E. Dagotto, Science **283**, 2034 (1999).

[6] A. Nucara, A. Perucchi, P. Calvani, T. Aselage, and D. Emin, Phys. Rev. B **68**, 174432 (2003).

[7] P. W. Anderson and H. Hasegawa, Phys. Rev. **100**, 675 (1955).

[8] P. G. de Gennes, Phys. Rev. **118**, 141 (1960).

[9] M. Quijada, J. Černe, J. R. Simpson, H. D. Drew, K. H. Ahn, A. J. Millis, R. Shreekala, R. Ramesh, M. Rajeswari, and T. Venkatesan, Phys. Rev. B **58**, 16093 (1998).

[10] V. A. Amelitchev, B. Güttler, O. Yu. Gorbenko, A. R. Kaul, A. A. Bosak, and A. Yu. Ganin, Phys. Rev. B **63**, 104430 (2001).

[11] P. Dai, J. A. Fernandez-Baca, E. W. Plummer, Y. Tomioka, and Y. Tokura, Phys. Rev. B **64**, 224429 (2001).

[12] A. J. Millis, R. Mueller, and B. I. Shraiman, Phys. Rev. B **54**, 5389 (1996); **54**, 5405 (1996).

[13] T. V. Ramakrishnan, H. R. Krishnamurthy, S. R. Hassan, and G. Venketeswara Pai, Phys. Rev. Lett. **92**, 157203 (2004).

[14] A. J. Millis, B. I. Shraiman, and R. Mueller, Phys. Rev. Lett. **77**, 175 (1996).

[15] O. Cépas, H. R. Krishnamurthy, and T. V. Ramakrishnan, Phys. Rev. Lett. **94**, 247207 (2005).

[16] Y.-L. Lee and Y.-W. Lee, Phys. Rev. B **75**, 064411 (2007).

[17] M. Stier and W. Nolting, Phys. Rev. B **75**, 144409 (2007).

[18] R. Yu, S. Dong, C. Şzen, G. Alvarez, and E. Dagotto, Phys. Rev. B **77**, 214434 (2008).

[19] C. Lin and A. J. Millis, Phys. Rev. B **78**, 174419 (2008).

[20] J. Zaanen, G. A. Sawatzky, and J. W. Allen, Phys. Rev. Lett. **55**, 418 (1985).

[21] M. B. J. Meinders, H. Eskes, and G. A. Sawatzky, Phys. Rev. B **48**, 3916 (1993).

[22] W. G. Yin, D. Volja, and W. Ku, Phys. Rev. Lett. **96**, 116405 (2006).

[23] P. Phillips, Rev. Mod. Phys. **82**, 1719 (2010).

[24] A. Rusydi, R. Rauer, G. Neuber, M. Bastjan, I. Mahns, S. Müller, P. Saichu, B. Schulz, S. G. Singer, A. I. Lichtenstein, D. Qi, X. Gao, X. Yu, A. T. S. Wee, G. Stryganyuk, K. Dörr, G. A. Sawatzky, S. L. Cooper, and M. Rübhausen, Phys. Rev. B **78**, 125110 (2008).

[25] W. E. Pickett and J. D. Singh, Phys. Rev. B **53**, 1146 (1996).

[26] A. Georges, G. Kotliar, W. Krauth, and M. J. Rozenberg, Rev. Mod. Phys. **68**, 13 (1996).

[27] If the double-exchange (DE) interactions were not there, each of the pairs of 4-5, 6-7, and 8-9 would merge into one. The 4-5 pair corresponds to the lower part of the JT-split states, while the 6-7 and 8-9 pairs correspond to the upper part. The 6-7 and 8-9 pairs are further split by the Coulomb repulsion (U_{eff}) between lower and upper JT-split states. Namely, when the lower JT-split level (4-5) is unoccupied, the upper level is given by 6-7, whereas if 4-5 is occupied, the corresponding upper level is given by 8-9.

[28] C. Ederer, C. Lin, and A. J. Millis, Phys. Rev. B **76**, 155105 (2007).

[29] If one shifts μ^* but remains around the valley, or changes the value of Γ from 0.1 to 0.6 eV, the effect of weight transfer is still captured with the crossover between regions of medium and high energy being relatively unchanged (within 1 eV), while the amount of weight transferred may change by not more than 100%.

[30] Since the self-consistently computed chemical potentials (μ) we found for the PM and FM phases are almost the same, we choose to define μ^* in PM and FM phases by shifting their corresponding μ to the left by the same amount. This way, μ^* for PM and FM phases are pretty much the same.